

# Chapter 9

## Numerical and Experimental Investigation of Aerodynamic Characteristics of an Unmanned Aerial Vehicle in a Low Subsonic Wind Tunnel



Furkan Dilbaz, Adnan Burak Incedal, Talha Batuhan Korkut, Yasemin Nur Aydın, Seda Kırmacı Arabacı, and Aytac Gören

### Nomenclature

$\rho$	Fluid density
$P$	Pressure
$\mu$	Coefficient of dynamic viscous
$u_i$	Fluctuating velocity
$G_\omega, G_k$	The formation of kinetic energy of turbulent and specific dissipation
$\Gamma_k, \Gamma_\omega$	Diffusivity
$S_k, S_\omega$	Source terms
$Y_k, Y_\omega$	Dissipation
$u_T$	The friction velocity
$\tau_w$	The wall shear stress
$C_f$	The skin friction coefficient
$u_i$	Fluctuating velocity
$\nu$	The kinematic viscosity
$V$	The flight speed
$c_{root}$	The length of root chord
$\lambda$	Taper ratio
$c_{tip}$	The length of tip chord
$C_L$	Aerodynamic lift coefficient
$C_D$	Aerodynamic drag coefficient

---

F. Dilbaz · A. B. Incedal · Y. N. Aydın · S. K. Arabacı  
Department of Mechanical Engineering, Celal Bayar University, Manisa, Turkey  
e-mail: [seda.kirmaci@cbu.edu.tr](mailto:seda.kirmaci@cbu.edu.tr)

T. B. Korkut · A. Gören (✉)  
Department of Mechanical Engineering, Dokuz Eylül University, Izmir, Turkey  
e-mail: [aytac.goren@deu.edu.tr](mailto:aytac.goren@deu.edu.tr)

## 9.1 Introduction

### 9.1.1 Literature Investigations

Unmanned aerial vehicles (UAV) are widely preferred today in the field of military and civil aviation due to parameters, such as ease of use, cost, life safety, and operational advantages (Ehrhard 2010). With the start of working on the UAV in the World War I and the increased interest in cruise missiles in the World War II, the interest in the UAV culture had increased rapidly (Keane and Carr 2013). In favor of the UAV, during the war, the crew was not damaged, and the opportunity of observation and data flow, as well as the opportunity to attack with the ammunition it could carry within its load-carrying capacity, was provided. In order to meet the military and civilian demands of the UAVs, which have been actively developing since the World War I, different designs are modeled according to the environmental conditions. While continuing the development of UAVs plays an active role in the war, UAVs are at the entrance of the Turkey market in the 2000s (Kahvecioglu and Oktal 2016). Following Bayraktar UAV, which was the first Turkish design and production of the Mini UAV system in 2006, the Turkish UAV market has grown with designs, such as Anka, Keklik, Gözcü, Turna, and Malazgirt (Kahvecioglu and Oktal 2016).

Unmanned aerial vehicles in both the world and Turkey aviation industry sector continue to work unabated. As time is processed, improvements are made in many parameters, such as aerodynamics, strength, lightweight, and fuel savings on the UAV. It is very important to examine the aerodynamic effects on aircraft such as UAVs, in order to reveal the change due to the air effect during the movement of the aircraft. In addition to military use, aerodynamic studies of single-rotor or multi-rotor drone UAVs, which are accepted as small aircraft in the literature in commercial use, are also continuing (Ventura Diaz and Yoon 2018). Vuruskan et al. defined the TURAC transition-flight mathematical model of the unmanned aerial vehicle (UAV) and examined the aerodynamic effects on CFD to define transition-flight regimes and aerodynamic coefficients (Vuruskan et al. 2014). Kapseong Ro and Kaushik Raghu analyzed the aerodynamic study of the free-wing tilt-body concept using the mathematical panel method and compared it with the experimental wind tunnel results (Ro et al. 2007). Wisnoe et al. examined the effect of different Mach numbers on aerodynamic lift coefficient ( $C_L$ ), drag coefficient ( $C_D$ ), and pitching moment coefficient ( $C_M$ ) values on the blended wing body (BWB) aircraft designed at MARA University of Technology (UiTM; Wisnoe et al. 2009). Funes-Sebastián and Ruiz-Calavera examined the effect of wind tunnel test walls on the Eikon model, a high-transonic UAV prototype, and compared the experimental data with CFD numerical results (Funes-Sebastian and Ruiz-Calavera 2014). Pattison et al. produced 5 degrees of freedom hardware equipment suitable for the wind tunnel so that the maneuvering movements of aircraft models could be analyzed experimentally (Pattinson et al. 2013). In addition to these studies, aerodynamic studies were carried out on models such as medium-altitude long-endurance (MALE) unmanned aerial vehicle (UAV) (Panagiotou et al. 2014, 2016), quad tilt-wing VTOL (Vertical Take-Off and Landing) UAV (Muraoka et al. 2009), quadrotor UAV (Dong et al. 2013), and a twin-engine tail-sitter unmanned air vehicle (UAV) (Stone 2002).

In order for the experiment to reflect the real conditions in the wind tunnel, the geometry to be examined must be proportionally reduced. While reducing the geometry, blockage rates are calculated based on the dimensions of the experimental setup. So as to examine the effect of blockage rate on aerodynamic terms such as the pressure distribution and the drag coefficient, studies were first conducted on simple geometries. To observe the aerodynamic effects of more complex models, computational fluid dynamics (CFD) package programs have become widespread in order to obtain a faster and more economical solution. Some articles on calculating the blockage can be listed as follows:

West and Apelt experimentally demonstrated the effect of different blockage rates in the range of 2–16% on pressure distribution, the drag coefficient, and Strouhal number on a circular cylinder (West and Apelt 1982). Perzon discussed the effect of two different geometric parameters on the blockage ratios and emphasized that the effect of the windscreen angle on blockage ratios was critical, while the effect of the front radius was not sensitive. Subsequently, the effect of blockage rates on a full-scale car was analyzed on CFD analysis and a slotted wall wind tunnel was modeled (Perzon 2001). Lian analyzed the effect of sidewall and blockage rate on flapping wing with different domain sizes numerically and interpreted aerodynamic forces and reduced pitching frequencies due to different blockage rates (Lian 2010). Ross and Altman discussed the aerodynamic effects of rotating disordered flow of rotating vertical axis wind turbines on the wake and solid blockage rate in the wind tunnel test environment (Ross and Altman 2011). Chen and Liou investigated the factors that are affecting the blockage ratio in their studies. According to the results obtained from the experimental setups with and without rotors, they determined that the rotor-type speed ratio, the blade pitch angle, and the tunnel blockage ratio had a direct effect on the blockage rate (Chen and Liou 2011). Altinisik et al. examined and compared aerodynamic effects on passenger cars numerically and experimentally. After verifying their experimental studies on wind tunnel with computational fluid dynamics (CFD), they examined the effects of different blockage ratios through CFD studies (Altinisik et al. 2015). Mokhtar and Hasan examined the wall interference effect that occurs with the different blockage rates on the same geometry on the computational fluid dynamics (CFD) package program (Mokhtar and Hasan 2016). Latif et al. examined the aerodynamic analysis of the tail sweep 45° effects of the UAV baseline 5 model, which was 71.5% reduced, by calculating solid blockage, wake blockage, and streamline curvature blockage corrections (Abd Latif et al. 2017).

## 9.1.2 Mathematical Formulations

### 9.1.2.1 Governing Equations

#### Continuity Equation and Navier-Stokes Equations

For UAV analyses, the flow is accepted to be incompressible through the speed of 40 m/s.

For this reason, the Navier-Stokes equations are solved at the same time with the k- $\omega$  SST and the continuity equation. The motion of incompressible Newtonian

fluid forms the continuity equation and momentum conservation equation (Wilcox 1998).

$$\frac{\partial \rho}{\partial t} + \frac{\partial(\rho u_i)}{\partial x_i} = 0 \quad (9.1)$$

$$\frac{\partial(\rho u_i)}{\partial t} + \frac{\partial(\rho u_i u_j)}{\partial x_j} = -\frac{\partial P}{\partial x_j} + \frac{\partial}{\partial x_j} \left( \mu \frac{\partial u_i}{\partial x_j} - \overline{\rho u_i u_j} \right) + S_j \quad (9.2)$$

$u_i$  and  $u_j$  ( $i, j = 1, 2, 3$ ) are components of the time-averaged velocity;  $\rho$  is the fluid density,  $P$  is the pressure of time-averaged,  $\overline{\rho u_i u_j}$  is the Reynolds stress,  $\mu$  is the coefficient of dynamic viscous;  $S_j$  is the translation of the source used in the momentum equation.

The Reynolds-averaged Navier-Stokes equations are the most recently used turbulence modeling in CFD. In that approach, the Navier-Stokes equations are decomposed into ensemble-averaged or time-averaged and floating components. The total velocity  $u_i$ ,  $\overline{u_i}$  mean velocity,  $u_i'$  is fluctuating velocity as given in the below equation.

$$u_i = \overline{u_i} + u_i' \quad (9.3)$$

### Turbulence Model Equations

Turbulence model selection depends on the grid type, i.e., for the structured grid as the present simulation, the SST model has been used. Standard the two-equation models exude the separation and predict foreboded flow even pressure gradient flows. However, the SST model is one of the specific two-equation models for separation estimation and also makes advantageous calculations of even more flowing wall-flow which highly separated regions. This model is correct than k-epsilon particularly near-wall layer, for flow with acceptable reverse pressure gradients (Menter et al. 2003; Menter 1992).

The following equations (which are in the form of Cartesian tensor) are called as the Reynolds-averaged Navier-Stokes (RANS) equations.

$$\frac{\partial(\rho u_i)}{\partial t} + \frac{\partial(\rho u_i u_j)}{\partial x_j} = \frac{\partial \rho}{\partial x_i} + \frac{\partial}{\partial x_j} \left[ \mu \left( \frac{\partial u_i}{\partial x_j} + \frac{\partial u_j}{\partial x_i} - \frac{2}{3} \delta_{ij} \frac{\partial u_k}{\partial x_k} \right) \right] + \frac{\partial}{\partial x_i} \left( -\overline{\rho u_i u_j} \right) \quad (9.4)$$

The Boussinesq hypothesis is adapted with the Reynolds stress and mean velocity;

$$-\overline{\rho u_i u_j} = \mu_t \left( \frac{\partial u_i}{\partial x_j} + \frac{\partial u_j}{\partial x_i} \right) - \frac{2}{3} \left( \rho k + \mu_t \frac{\partial u_k}{\partial x_k} \right) \delta_{ij} \quad (9.5)$$

The SST  $k-\omega$  is the combination of Wilcox  $k-\omega$  model and the standard  $k-\epsilon$  model. The shear-stress transport (SST) was developed by Menter (1994).

The shear-stress transport (SST)  $k-\omega$  model nearly integrated the certain formulation of the  $k-\omega$  model in the near-wall zone with the free-stream determination of the  $k-\omega$  model in the far domain. The standard  $K-\omega$  model captures the effects on the outer layer as well as the lower viscous layer effects on the inner layer.

Coupling of transition model with SST  $k-\omega$  by modification of  $k$  equations is given as follows,

$$\frac{\partial}{\partial t}(\rho k) + \frac{\partial}{\partial x_i}(\rho k u_i) = \frac{\partial}{\partial x_j} \left( \Gamma_k \frac{\partial k}{\partial x_j} \right) + G_k - Y_k + S_k \quad (9.6)$$

$$\frac{\partial}{\partial t}(\rho \omega) + \frac{\partial}{\partial x_j}(\rho \omega u_j) = \frac{\partial}{\partial x_j} \left( \Gamma_\omega \frac{\partial \omega}{\partial x_j} \right) + G_\omega - Y_\omega + D_\omega + S_\omega \quad (9.7)$$

$G_\omega$  and  $G_k$  are the formations of the kinetic energy of turbulent and specific dissipation.  $\Gamma_k$  and  $\Gamma_\omega$  are diffusivity,  $Y_k$  and  $Y_\omega$  are dissipation, and  $S_k$  and  $S_\omega$  are source terms. For standart  $k-\epsilon$  and  $k-\epsilon$  model,  $D_\omega$  is extra-diffusion term, which is the function of blending.

$$D_\omega = 2(1 - F_1) \rho \sigma_\omega \omega + \frac{1}{\omega} \frac{\partial k}{\partial x_j} \frac{\partial \omega}{\partial x_j} \quad (9.8)$$

## 9.2 Material and Method

### 9.2.1 UAV Design Similar Model with Anka UAV

The Anka-like UAV models, which are inspired by the Turkish Anka unmanned aerial vehicle (UAV) geometry, are analyzed in the CFD program and compared with the experimental data. The TAI Anka is an unmanned aerial vehicle developed by Turkish Aerospace Industries (TAI) for the Turkish Armed Forces. In this study, the UAV model is designed and imported into a 3D package CAD program, and surfaces are generated. The designed model is shown in Fig. 9.1.

The geometry of the main wing has a span of 9 m and a NACA4415 airfoil at the wingtip, NACA 2412 airfoil at tail fuselage length is 8.13 m, and the wing MAC, aspect ratio, taper ratio, wing area, projected area, the volume of UAV, respectively, are 0.91, 9.83, 0.4698, 7.97 m<sup>2</sup>, 2.24 m<sup>2</sup>, and 5.63 m<sup>3</sup>.

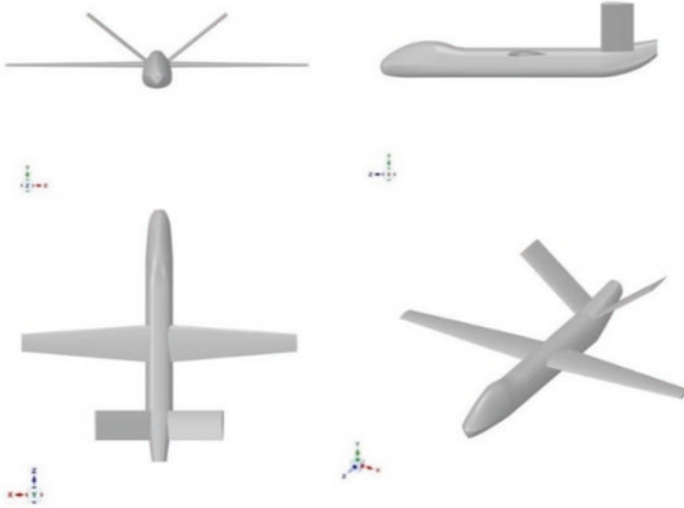


**Fig. 9.1** Anka-like UAV model

## 9.2.2 Numerical Setup on ANSYS: Computational Fluid Dynamics (CFD) Package Program

### 9.2.2.1 Brief Description of Analysis

Firstly, different lengths of wingspan are compared, the effects of wing lengths on the drag coefficient are investigated, and depending on the wingspan, the stability of drag coefficient is examined. Since it will be

compared with wind tunnel tests, the most efficient length will be determined to fit into the tunnel. This length will be chosen where the pressure acting on the wall is the minimum and the length most suitable for the tunnel in terms of size. The wing's length reduction study is carried out to obtain a drag coefficient stability of the wings for the designs with 17-meter wing lengths in the wind tunnel test room. Firstly, the drag coefficient changes of the existing models according to the wing lengths are examined. The variations of  $C_D$  with these measurements are determined on the results obtained with 0, 5, 7, 8, 9, 11, 13, and 17 m. The pressure and drag coefficients of the model in the tunnel test chamber are compared according to the optimum wing lengths. Determined into the existing control domain, the models are placed in smaller sizes. For blockage approach, analyses are made in 6 different sizes for the Anka-like UAV. Before the experimental study, CFD analysis was performed on the UAV test model to specify the correct scale for the unmanned aerial vehicle. While determining the test scale, the following factors were taken into consideration. Pressure-position graphs were obtained by increasing wing lengths by 20 cm at 40 m/s. These wing structures, which are created by increasing 20 cm, have the ratio of the body to 1/39, 1/40, 1/42, 1/52, 1/59, 1/69 scale, respectively

The resulting drag coefficients, lift coefficients, and aerodynamic efficiencies are then averaged to obtain the drag at a given angle of attack as 0, 4, 8, 12, and 16 degrees in CFD. For the angle of attack  $+4^\circ$  drag coefficient of the Anka-like UAV which length is 8 m, wingspan is 17.3 m was found to be 0.06 in  $3.45 \times 10^6$  Reynolds number in CFD (Kırmacı Arabacı and Dilbaz 2019). The lift and drag measurements are corrected to account for the effects of wake blockage, solid blockage, and streamline curvature.

### 9.2.2.2 Grid Independence Check

One of the most important issues in computational fluid dynamics is the mesh. Depending on the number and quality of the mesh, the results can be different. Grid independence study is carried out varying of the mesh size. The Navier-Stokes equations are solved, assuming incompressible flow and Steady-state. The mesh independence study is performed at a speed of 40 m/s using the K- $\omega$  SST turbulence model. Small boxes are created around the UAV in the domain. The Anka-like UAV mesh is actualized in the range of 2 million–24 million. Figure 9.2 shows the size of the mesh elements of the cell grid. Results show that 21 million mesh can be chosen as the converged for this study. The grid was quite sufficient to capture the results.

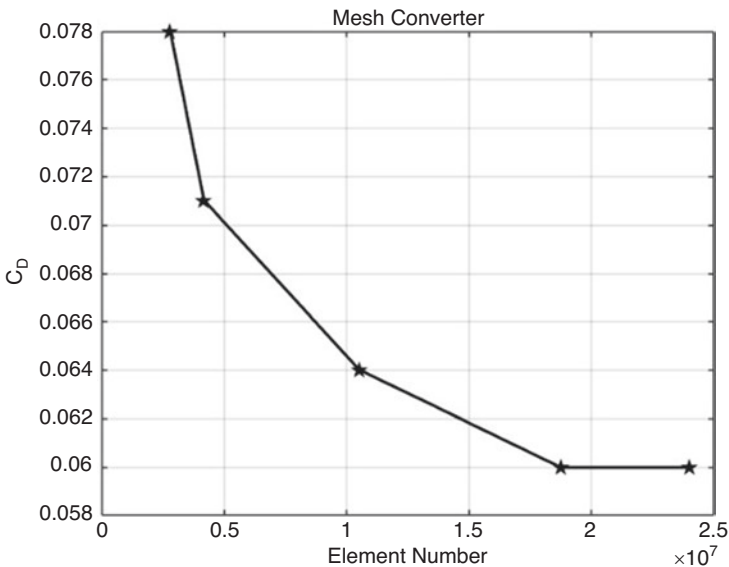
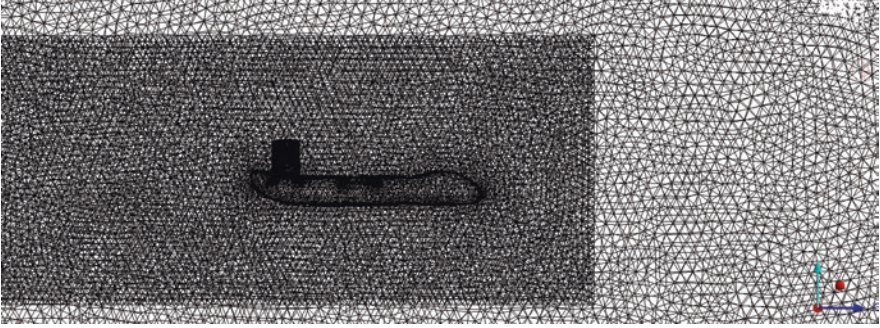


Fig. 9.2 Grid independence results



**Fig. 9.3** Meshing of the Anka-like UAV

### 9.2.2.3 Boundary Conditions

The test model was imported into the ANSYS-FLUENT environment for meshing. In Fig. 9.3, control volumes are formed around the models.

The computational domain is selected after a comprehensive evaluation. In this study, the fuselage axis of each model is considered as the axis of symmetry, the control volume is placed 3 aircraft lengths away from the air intake surface and 6 aircraft lengths away from the air outlet surface, and 2.5 aircraft wings were left on the right side for 1/1 scale. For other scales, the control domain is selected as the room sizes of the wind tunnel.

The body of influence region to the models has high grid density, and taken by surround a layer of very fine mesh. In the outlet zone, the density of the mesh is progressively increased, so it is coarse as it goes outer far from the surface of models. The wall functions have confidence in the comprehensive law of the wall, which actually states the velocity dispersion near to a wall is similar for nearly all turbulent flows. One of the most significant parameters when appreciating the applicability of the wall functions is called dimensionless wall distance ( $y^+$ ), demonstrated by Schlichting and Gersten (2016). Turbulent flows are remarkably affected by the asset of walls, where viscosity influenced regions have large gradients in the solution variables, but exactly calculating regions near the wall is very significant for accomplished estimation of wall-related flows (Gerasimoc 2006; Menter 1993).

For this case, the boundary layer thickness should be resolved in CFD problems. The first boundary layer thickness determined as inflation in the analysis calculated with the equation is as follows. The boundary layer thickness of the analysis to be solved with the Reynolds-averaged Navier-Stokes simulation (RANS) model in a computational fluid dynamics solver must first be calculated.

$$y^+ = \frac{yu_T}{\nu}; u_T = \sqrt{\frac{\tau_w}{\rho}}, \tau_w = 0.5C_f\rho U_\infty^2; C_f = 0.0576\text{Re}_d^{-\frac{1}{5}} \quad (9.9)$$



As a result of the equations, the Reynolds number is calculated primarily to find the boundary layer thickness.  $u_T$  is the friction velocity,  $\tau_w$  is the wall shear stress,  $C_f$  is the skin friction coefficient,  $y$  is the absolute distance (it is from the Wall), and  $\nu$  is the kinematic viscosity.

Before starting to calculate, a  $y$  value is determined, and accordingly, the height of the first element is calculated by friction velocity and kinematic viscosity (Bredberg 2000). In this study, the first boundary layer thickness  $y$  was found by taking  $y^+ = 1$ . It is observed that the  $k-\omega$  SST (shear-stress transport) model performs better in regions with flow separation compared to the other turbulence models. The  $k-\omega$  SST turbulence model was used in analyses to model the flow in areas where there may be flow separation with the lowest possible error (Menter 1993).  $21 \times 10^6$  tetrahedral elements were used for the Anka-like meshing, and the  $C_L$  and  $C_D$  coefficients are calculated in a  $y^+ \approx 1$  for 1/1 scale. With respect to the heights of the first element, the inflation layers are conceived on models, and 3D control volumes are created on every side boundary region. It is important to attention of  $y^+$  in order to capture the flow separation.

The first element heights of inflation layers are calculated, and, according to the  $y^+$  value which is equal to 1, the first element heights are created. The cell properties for the 1/1-scale Anka-like UAV model are as follows: 9 m length, first layer height is  $9.347 \times 10^{-6}$ , inflation layer is 6, maximum skewness is 0.83, minimum orthogonal quality is  $9.0856 \times 10^{-2}$ , and element number is 21245756.

The Reynolds number is found using the mean aerodynamic chord (MAC); MAC is denoted by  $\bar{c}$ ,  $V$  is the flight speed,  $c_{root}$  is the length of root chord,  $\lambda$  is the taper ratio, and  $c_{tip}$  is the length tip chord. All of the conditions are in-flight conditions.

$$Re = \frac{\rho V \bar{c}}{\mu} \quad (9.10)$$

$$\bar{c} = \frac{2}{3} * c_{root} * \left( \frac{1 + \lambda + \lambda^2}{1 + \lambda} \right) \quad (9.11)$$

$$\lambda = \frac{c_{tip}}{c_{root}} \quad (9.12)$$

The boundary conditions of UAVs are defined as a wall and no-slip conditions. Air velocity is accepted as 40 m/s for 1/1 scale in the inlet, the outlet is defined as the pressure outlet, and 0 Pa is taken. The 1/40 scale, the UAVs, and sides are taken wall and defined no-slip conditions like the wind tunnel. The turbulence intensity is set at 1.29%, and the turbulence viscosity ratio is 5 in CFD. The flow is incompressible; a pressure-based solver is used. It is chosen for the low-altitude flight regime as subsonic.

The parameters, which are the outlet pressure, inlet viscosity, and density of air, are received at sea-level conditions for analysis. The density and temperature are,

respectively,  $1.225 \text{ kg/m}^3$  and  $15.5 \text{ }^\circ\text{C}$ , while the dynamic viscosity is  $1.789 \times 10^{-5} \text{ kg/ms}$ .

The sides of the control volume are defined as a wall. The reason for this is wind tunnel tests, and analyses should be under the same boundary conditions. The experiments are performed in the Manisa Celal Bayar University open-return sub-sonic wind tunnel.

#### 9.2.2.4 Dynamic Similarity

To ensure geometric similarity, the sizes of the model should be proportional to that of the prototype. The Reynolds number must be checked for dynamic similarity. The Reynolds number of the test model and its prototype have to be calculated equally. The Reynolds number independence was obtained in all of the experimental work.

The maximum wind speed in the test section is  $40 \text{ m/s}$ , and the length of the wind tunnel is  $1 \text{ m}$ . In Eq. 9.13, the dynamic similarity studies have been performed, and then the scaling factor has been obtained. It was decided to continue the studies on a  $1/40$ -scale model.

$$\text{Re}_{1/40} = \frac{40 \times \bar{C}_{1/40}}{\nu} = R_{1/1} = \frac{U_\infty \times \bar{C}_{1/1}}{\nu} \quad (9.13)$$

Before the numerical and experimental studies, critical flow regions should be determined on the relevant test model, and the differences in these regions as a result of the analysis should be interpreted on the accuracy of the relevant numerical test methods. Specified critical flow regions on the Anka-like UAV model is shown in Fig. 9.4. On the Anka-like UAV model, there are three specified regions to the comparing numerical results. These regions are determined in line with the regions where flow separations are intense. The pressure distributions, drag force and lift force obtained as a result of the computational fluid dynamics (CFD) analysis of the test models obtained as a result of dynamic similarity are shown in Table 9.1 and Fig. 9.5. According to the results, a  $1.33\%$  difference was obtained between  $1$ -scale and  $40$ -scale test models. When the pressure distributions over the critical regions are examined, a  $1.75\%$  difference occurs.

#### 9.2.2.5 Pressure Distribution Between the Anka-Like UAV Model

Before the experimental study, CFD analysis was performed on the UAV test model to specify the correct scale for the unmanned aerial vehicle. While determining the test scale, the following factors were taken into consideration (Korkut and Goren 2020; Cook 1978; Pettersson and Rizzi 2008):

1. Test models must be able to be positioned in the wind tunnel test section.

**Fig. 9.4** Specified critical flow regions on the Anka-like UAV model

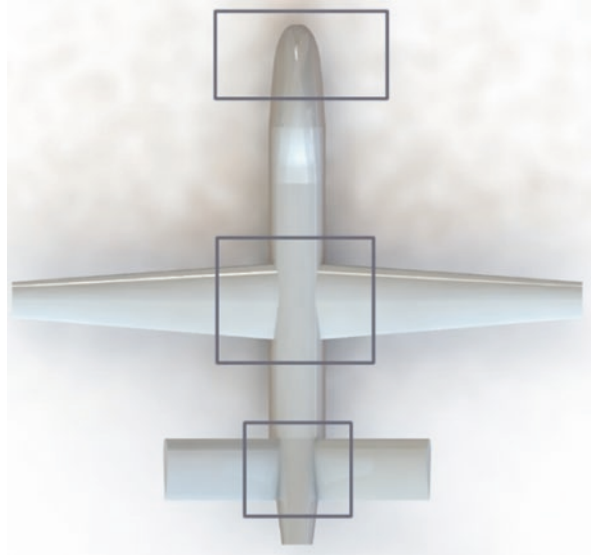


**Table 9.1** Dynamic similarity studies of the Anka-like UAV model

Model	Scale	V [m/s]	$F_D$	$F_L$	$C_D$	$C_L$
Anka-like	1/1	1	0.34	1.2	0.069	0.245
	1/40	40	0.33	1.1	0.069	0.232

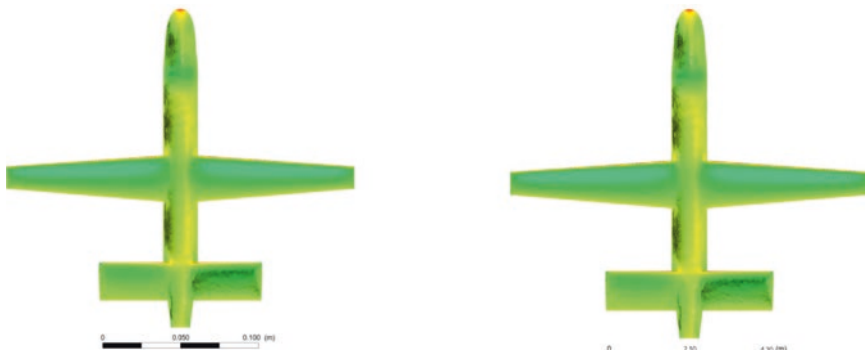


**Fig. 9.5** The dynamic similarity comparison of 1/1 and 1/40 models

2. The test model has to be scaling with the blockage ratio of the wind tunnel.
3. The airflow beyond the borders of the scaled test model should return to the normal behavior as it approaches the test section walls of the wind tunnel.

The x-axis of the graphics in Fig. 9.6 expresses the symmetrical width of the wind tunnel test chamber. On the x-axis presented in the graph, the value 0 represents the test model and the test chamber center position, and the value 0.15

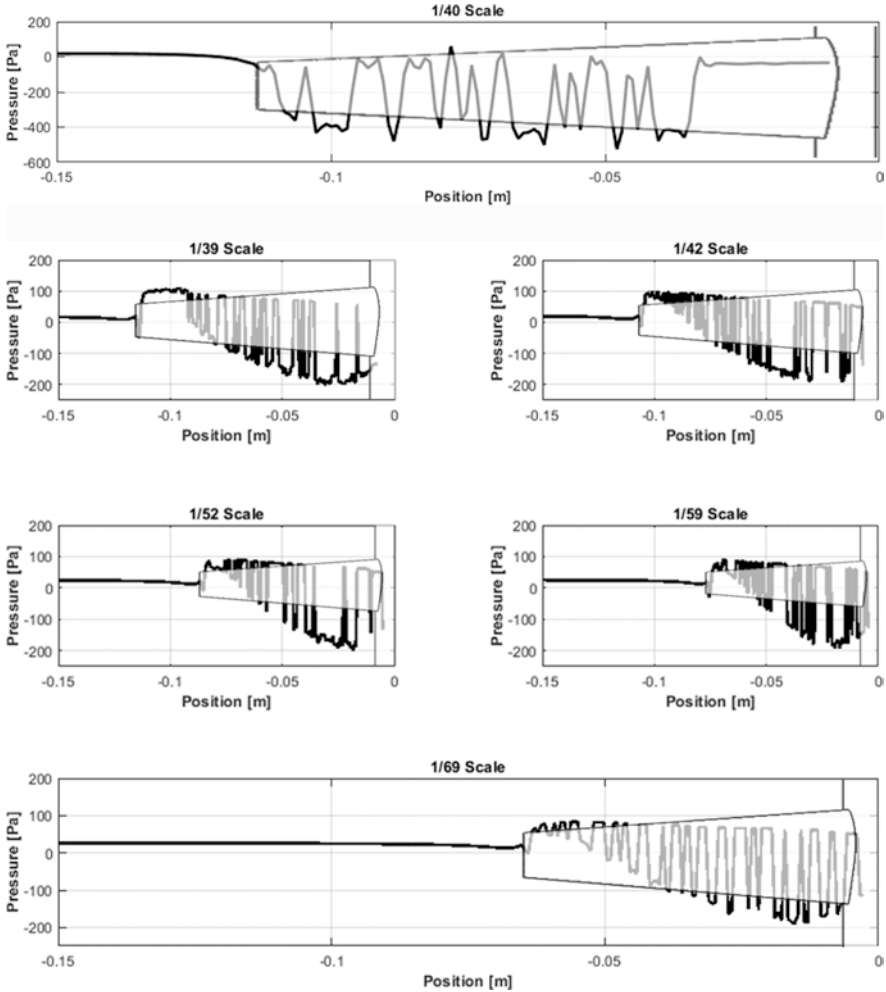


**Fig. 9.6** Pressure distribution between the Anka-like UAV and wall of the wind tunnel

represents the test chamber wall. All scaled test models meet the condition specified in Clause 3. As a result of the wind tunnel testing capabilities and dynamic similarity condition, it was decided to examine the most appropriate scale 1/40 in experimental studies.

As shown in Fig. 9.6, pressure distributions on the line, which is located on the wing, were obtained to specify the correct scale. The pressure difference is converged 3.5 cm away from the sidewalls of the wind tunnel on the 1/40-scale model of the UAV. Therefore, the appropriate scale has been chosen and ensured as a 1/40 scale. In this study, the blocking rate is 1.56% and in agreement with the literature (Boutillier and Yarusevych 2012).

### 9.2.3 Experimental Setup

The wind tunnel is an open-loop-type wind tunnel environment with general dimensions of 1500 mm × 2000 mm × 6500 mm as shown in Fig. 9.7. It is operated by a blower system supported by a 15kW motor with a 600 mm axial fan, which works at a maximum rev of 3000 rpm, as shown in Fig. 9.8. The maximum wind speed of the wind tunnel is created by 70 m/s (Arabacı and Pakdemirli 2016). The contraction ratio of the wind tunnel is 11.1.

Futek LSB200 Load Cell sensors are used for force measurement in the wind tunnel. The strain gauge is created by placing a thin resistor strip on an elastic material with a specific geometric design. It allows the measurement of the axial force on the elastic material with the effect of the load.

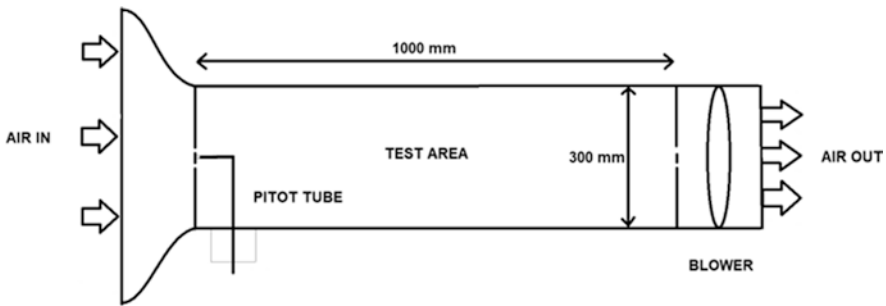
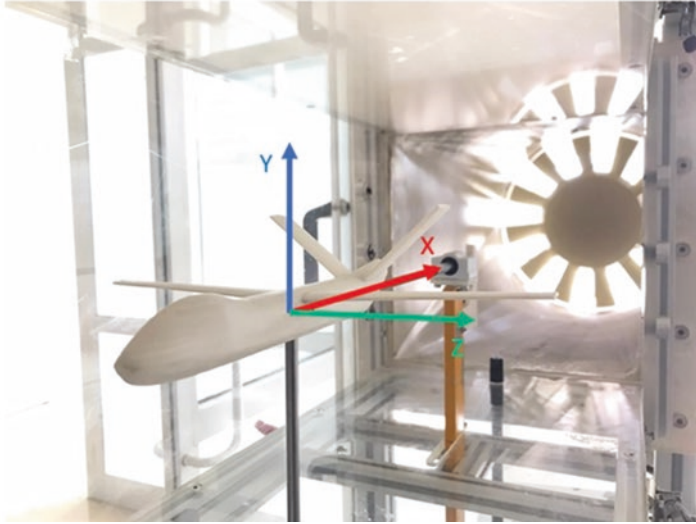


Fig. 9.7 Two-dimensional representation of the wind tunnel



Fig. 9.8 Manisa Celal Bayar University wind tunnel



**Fig. 9.9** Display of the supports of the test model produced with 3D printer in the experimental environment. (Turbotek n.d.)

In this study, the effects of the current with the force measurement mechanisms are designed for the x- and y-axis as shown in Fig. 9.9. Y-axis force measurement mechanism is created on the center of gravity of the test object to eliminate the mass forces. High-precision linear bearings and high-precision shafts are used in both axes to be measured, in order to eliminate the effects of the **undesirable** forces.

The connection between the test object and the force measurement mechanisms in the test room is provided with an 8 mm diameter shaft. Linear bearings are used in both axes to prevent misalignments. The data obtained from the sensors are recorded. The measurements are taken from the x- and y-axes during the experiments. After measurements are transferred to the LabView program, the data were processed and recorded. During the experiments, it is paid attention that there is not a strong wind, temperature changes, and pressure changes (rain, etc.) in the environment. Outdoor parameters are continuously observed and recorded.

The 1/40-scaled models used in the experiments are created by using 3D printers and PLA material with a 100% occupancy rate. Holes are drilled for shafts in the x- and y-axes, aligning from the center of

gravity. It has been sanded with fine sandpaper to remove the roughness of the surface gradually. After sanding, the models are spray-painted and varnished with spray varnish. In order to have the axial misalignment and angle of attack  $0^\circ$ , a spirit level is used after the assembly of the Anka-like model.

### 9.3 Results and Discussion

#### 9.3.1 Variation of Drag Coefficient According to Wingspan

In order to reveal the aircraft design suitable for the experimental test room, the drag coefficient graph based on the symmetry wingspan is presented in Fig. 9.10. The symmetry wingspan limits are kept between 17 m and 0 m. The symmetry wingspan range, which has stabilized the drag coefficient value, is considered to be suitable for the experimental environment. As shown in Fig. 9.10, it is observed that the drag coefficient is stable between 4.5 m and 5.5 m, and therefore, it is decided that the length suitable for the experimental environment should be 4.5 m for a single wing.

#### 9.3.2 Aerodynamic Performance of the Anka-Like Model for Different Reynolds Numbers at Angle of Attack=0°

As shown in Fig. 9.11, the ratio of  $C_L$  to  $C_D$ , which is an indication of aerodynamic efficiency, for an angle of attack value of 0° and for the range of the Reynolds number was investigated in this study. Increasing the Reynolds number reduces the drag, resulting in an increased aerodynamic performance of the Anka-like unmanned aerial vehicle. The experimental studies of the aerial vehicle aerodynamics with

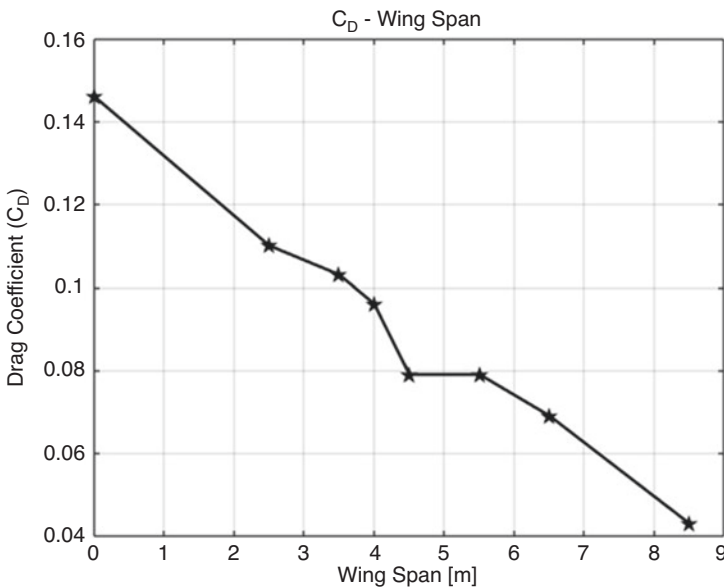
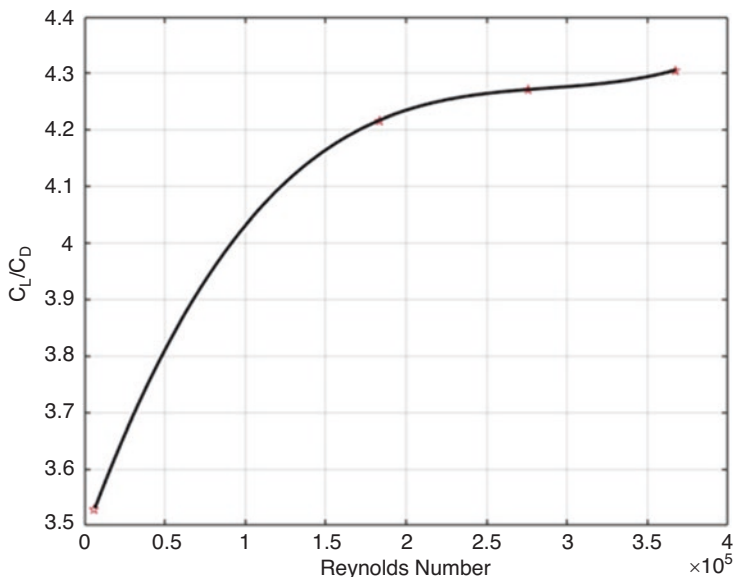


Fig. 9.10 Drag coefficient values depending on wingspan



**Fig. 9.11** Effects of the Reynolds number on  $C_L$  to  $C_D$  ratio for  $\alpha = 0^\circ$

1/1-scale prototypes are quite expensive and difficult. Therefore, the scaled test models are used in experimental studies. Before the preparation of the test model, there are some similarity rules for consideration. The ratios of the velocity vector on prototypes and models should be fixed for providing dynamic similarity.

Besides that, the dynamic similarity depends also on the blocking effect. The blockage ratio is defined as the ratio between the front sectional area of the test section and the test model. The blockage ratio is recommended to be below the 10% limit for the blocking effect to be neglected in the wind tunnel tests (Skalak et al. 1989; Ku 1997; Jones 1969).

### 9.3.3 Comparison of Experimental and Numerical Aerodynamic Coefficients

As shown in Table 9.2, experimental and numerical aerodynamic coefficients were compared in the 1/40-scale Anka-like model. As a result of this comparison, a 5.47% error value was observed between the experimental and numerical drag coefficient values, while a maximum error of 11% error was observed between the lift coefficient values. In this way, the experimental environment and the numerically modeled CFD environment have been verified.



**Table 9.2** Comparison with experimental and numerical aerodynamic coefficient results

Experimental drag coefficient ( $C_D$ ) values	0.073	5.47% error
Numerical drag coefficient ( $C_D$ ) values	0.069	
Experimental lift coefficient ( $C_L$ ) values	0.209	11% error
Numerical lift coefficient ( $C_L$ ) values	0.232	

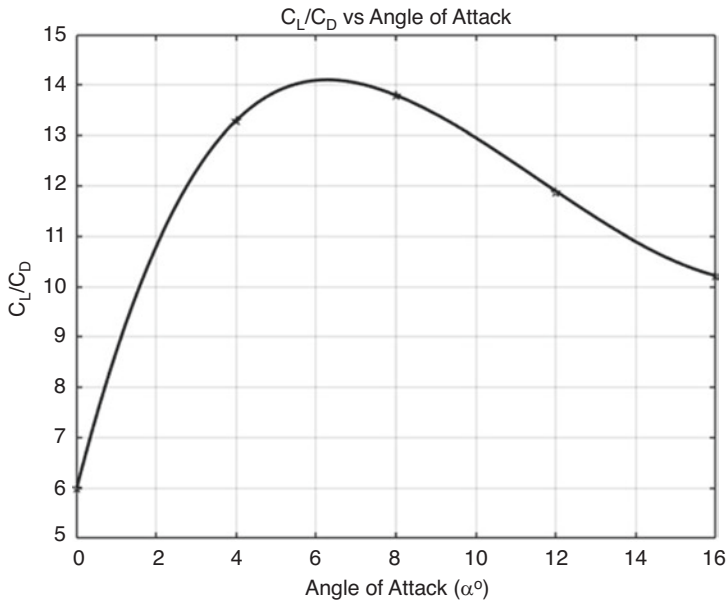


**Fig. 9.12** Graphic of  $C_L/C_D$ : angle of attack ( $\alpha^\circ$ )

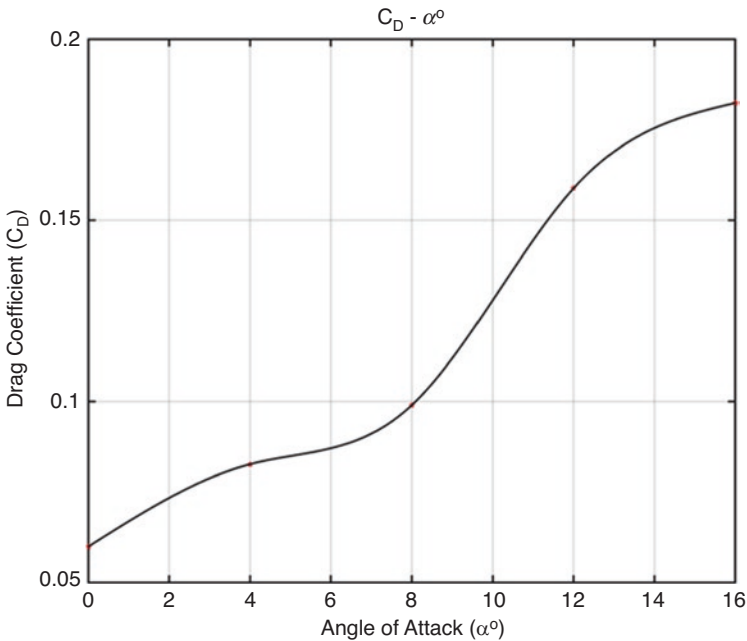
### 9.3.4 Change in Aerodynamic Efficiency Due to Angle of Attack

Figure 9.12 shows the variation of aerodynamic efficiency according to the angle of attack. Aerodynamic efficiency is an important design parameter in unmanned aircraft designs, and low drag is desired despite high lift. High aerodynamic efficiency means higher load-carrying capacity and lower thrust power. (The low drag of the aircraft against high lift means that it has a high load-carrying capacity and a lower thrust power.) This provides a better fuel economy, climbing performance, and glide rate in the aircraft. It is seen that the ratio of the lift coefficient to drag coefficient ( $C_L/C_D$ ) increases up to a certain angle of attack and decreases after this angle value.

The main reason for this is that, up to a certain angle of attack, the increase in the lift coefficient is higher than the drag coefficient. But after this critical angle value, aerodynamic efficiency begins to decrease. The most obvious reason for this situation is that flow separation starts over the wing and increases the drag. The highest  $C_L/C_D$  value was reached at  $6^\circ$ , and this value is 14.

### 9.3.5 Drag Coefficient ( $C_D$ ) Variation Depending on the Angle of Attack

The variation of drag coefficient ( $C_D$ ) according to the angle of attack is shown in Fig. 9.13. As the angle of attack increases, there is a continuous increase in the drag coefficient. As the stall angle is approached, the drag increases at a higher rate due to flow separation. At this critical angle of attack value, the highest drag coefficient is 0.182. The lowest drag coefficient was seen when the angle of attack was  $0^\circ$  and its value was 0.059.



**Fig. 9.13** Graph of  $C_D$ : angle of attack ( $\alpha^\circ$ )

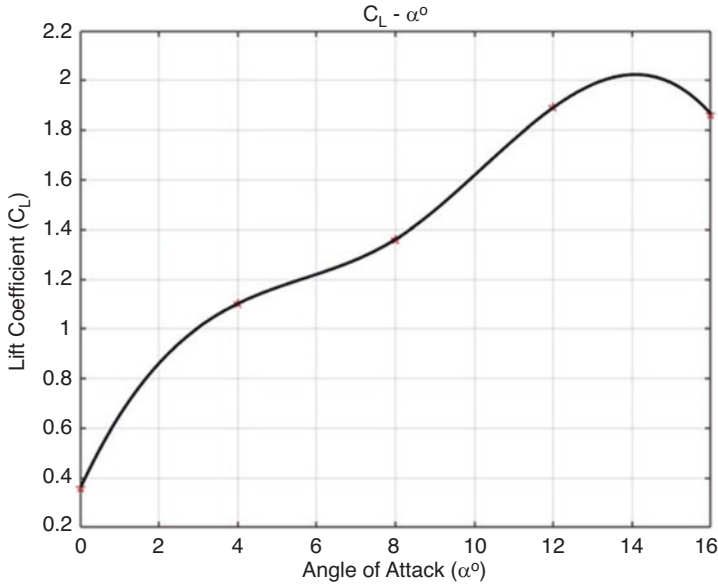


**Fig. 9.14** Graph of  $C_L$ : angle of attack ( $\alpha^\circ$ )

### 9.3.6 Lift Coefficient ( $C_L$ ) Variation Depending on Angle of Attack

The variation of the lift coefficient ( $C_L$ ) according to the angle of attack is shown in Fig. 9.14. Increasing the angle of attack also increases the lift coefficient. However, when the angle of attack is  $15^\circ$ , the lift coefficient decreases. At this angle, flow separation occurs on the wing. This causes a loss of lift in the wing. This critical angle of attack is called the stall angle. As it can be understood from the graph of the change of aerodynamic efficiency, according to the attack angle, when the angle of attack is  $12^\circ$ , the lift coefficient reaches its highest value, and this value is 1.89. On the other hand, the angle of attack has the lowest lift coefficient at  $0^\circ$ , and its value is 0.36.

### 9.3.7 Pressure Distribution and Vortex Core Region Results

Pressure distribution and vortex core regions are shown in Fig. 9.15. It was observed that the pressure change increases around the stagnation points on the wings and body. Pressure changes have calculated as 1 kPa around the wings and body. Sudden pressure change causes the vortex around the solid body. In continuum mechanics, vortex is a pseudovector field that describes the local spinning motion of a

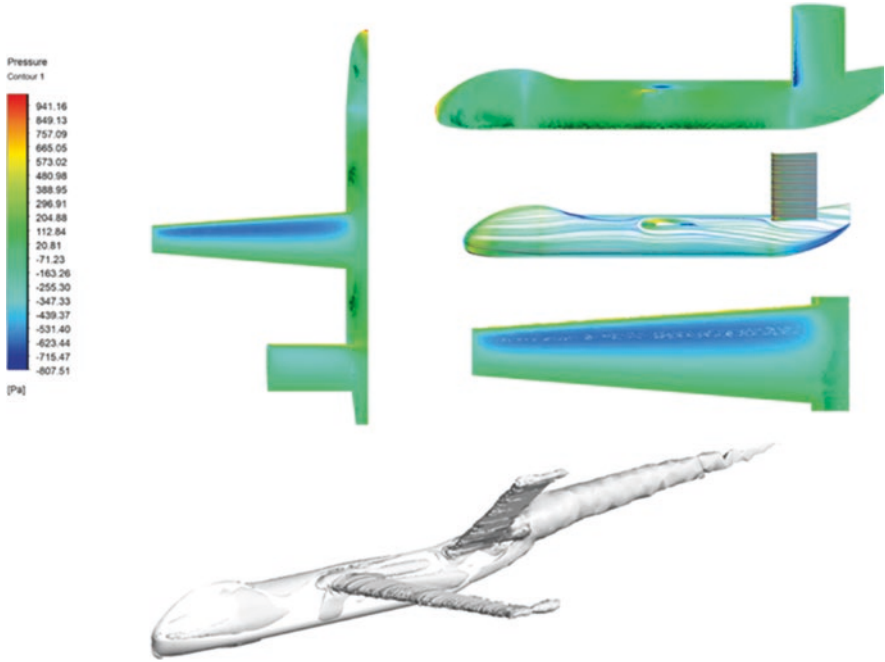


**Fig. 9.15** Pressure contours and vortex core regions on the Anka-like UAV model

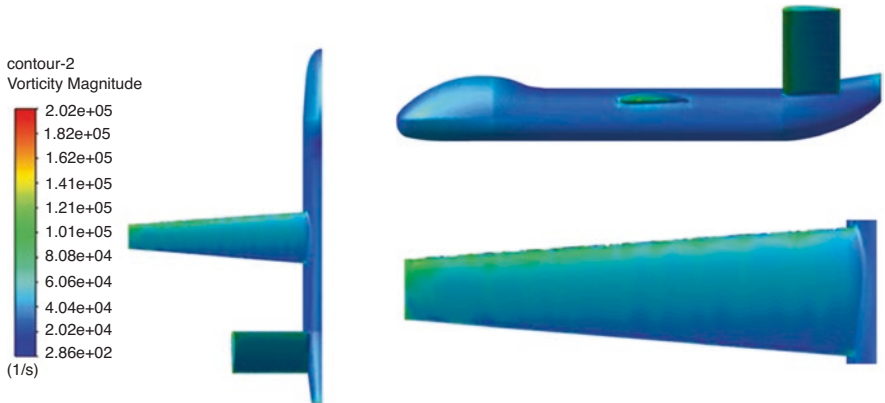


**Fig. 9.16** Vorticity magnitude changes on the Anka-like UAV model

continuum near some point, as would be seen by an observer located at that point and traveling along with the flow. It is an important quantity in the dynamical theory of fluids and provides a convenient framework for understanding a variety of complex flow phenomena, such as the formation and motion of vortex rings (Lecture Notes 2015; Moffatt 2015; Guyon et al. 2002). As shown in Fig. 9.16, the vorticity magnitude increased at the flow separation points and returned to the normal behavior on the body.

## 9.4 Conclusion

In this study, the aerodynamic effects of the similar model with the Anka model were examined in both experimental and numerical environments. On the model similar to Anka, aerodynamic coefficients due to different angles of attack, wingspan selection, dynamic similarities, aerodynamic effects according to different Reynolds numbers, experimental verification of the results, and the pressure distribution of models in different scales were examined. Several conclusions were drawn from this study as follows:

1. The drag coefficient value depending on the wingspan was examined, and the wingspan suitable for the experimental wind tunnel room was taken as 4.5 m from the range where the drag coefficient value was stable.
2. In order to select the scaled geometry suitable for the experimental environment, CFD analysis was performed in six different scales, and it was observed that the 1/40 scale with a blocking rate of 1.56% was suitable for the experimental environment.
3. In order to determine the aerodynamic performance of the designed model, aerodynamic coefficients depending on the angle of attack were determined. After increasing the lift coefficient up to the critical angle of attack, a decrease was observed. In the drag coefficient, the coefficient increased as the angle of attack increased.
4. Depending on the Reynolds number, an increase in  $C_L/C_D$  values was observed, but, as the Reynolds number was increased, the rate of increase was decreased.
5. It was found that the experimental results are in good agreement with the numerical solution in the  $C_D$  and  $C_L$  values of the 1/40-scale model.

## References

- Abd Latif, M.Z.A., Ahmad, M.A., Nasir, R.M., Wisnoe, W., Saad, M.R.: An analysis on 45 sweep tail angle for blended wing body aircraft to the aerodynamics coefficients by wind tunnel experiment. In: IOP Conference Series: Materials Science and Engineering, vol. 270, no. 1, p. 012001. IOP Publishing (2017, December)
- Altınisik, A., Kutukceken, E., Umut, H.: Experimental and numerical aerodynamic analysis of a passenger car: influence of the blockage ratio on drag coefficient. *J. Fluids Eng.* **137**(8) (2015)
- Arabacı S., Pakdemirli M.: Improvement of aerodynamic design of vehicles with inspiration from creatures, PhD Thesis, Department of Mechanical Engineering, Manisa Celal Bayar University (2016)
- Boutillier, M.S., Yarusevych, S.: Effects of end plates and blockage on low-Reynolds-number flows over airfoils. *AIAA J.* **50**(7), 1547–1559 (2012)
- Bredberg, J.: On the wall boundary condition for turbulence models. Chalmers University of Technology, Department of Thermo and Fluid Dynamics. Internal Report 00/4. Goteborg, pp. 8–16 (2000)
- Chen, T.Y., Liou, L.R.: Blockage corrections in wind tunnel tests of small horizontal-axis wind turbines. *Exp. Therm. Fluid Sci.* **35**(3), 565–569 (2011)

- Cook, N.J.: Determination of the model scale factor in wind-tunnel simulations of the adiabatic atmospheric boundary layer. *J. Wind Eng. Ind. Aerodyn.* **2**(4), 311–321 (1978)
- Dong, W., Gu, G.Y., Zhu, X., Ding, H.: Modeling and control of a quadrotor uav with aerodynamic concepts. In: *Proceedings of World Academy of Science, Engineering and Technology*, vol. 77, p. 437. World Academy of Science, Engineering and Technology (WASET) (2013)
- Ehrhard, T.P.: *Air Force UAV's: The Secret History*. Mitchell Institute for Airpower Studies Arlington VA. (Ehrhard, 2010) (2010)
- Funes-Sebastian, D.E., Ruiz-Calavera, L.P.: Numerical simulations of wind tunnel effects on intake flow of a UAV configuration. In: *52nd Aerospace Sciences Meeting*, p. 0372 (2014)
- Gerasimoc, A.: *Modelling Turbulence Flows with Fluent*. Europe ANSYS Inc. (2006)
- Guyon, E., Hulin, J.P., Petit, L., Mitescu, C.D., Jankowski, D.F.: Physical hydrodynamics. *Appl. Mech. Rev.* **55**(5), B96–B97 (2002)
- Jones, R.T.: Blood flow. *Annu. Rev. Fluid Mech.* **1**(1), 223–244 (1969)
- Kahvecioglu, S., Oktal, H.: Historical development of UAV technologies in the world: the case of Turkey. In: *Sustainable Aviation*, pp. 323–331. Springer, Cham (2016)
- Keane, J.F., Carr, S.S.: A brief history of early unmanned aircraft. *Johns Hopkins APL Tech. Digest.* **32**(3), 558–571 (2013)
- Kırmacı, A.S., Dilbaz, F.: Aerodynamic analysis of Anka UAV and Heron UAV. In: *2nd International Conference on Energy Research*, 11–13 April, Marmaris, Turkey (2019)
- Korkut, T.B., Goren, A.: Aerodynamic effect of wing mirror usage on the Solaris 7 solar car and demobil 09 electric vehicle. *Int. J. Automot. Mech. Eng.* **17**(2), 7868–7881 (2020)
- Ku, D.N.: Blood flow in arteries. *Annu. Rev. Fluid Mech.* **29**(1), 399–434 (1997)
- Lecture Notes from University of Washington, at the Wayback Machine, Archived 16 Oct 2015 (2015)
- Lian, Y.: Blockage effects on the aerodynamics of a pitching wing. *AIAA J.* **48**(12), 2731–2738 (2010)
- Menter, F.R.: Improved Two-equation k-omega Turbulence Models for Aerodynamic Flows. Nasa Sti/Recon Technical Report N, 93, 22809 (1992)
- Menter, F.: Zonal two equation kw turbulence models for aerodynamic flows. In: *23rd Fluid Dynamics, Plasmadynamics, and Lasers Conference*, p. 2906 (1993, July)
- Menter, F.R.: Two-equation eddy-viscosity turbulence models for engineering applications. *AIAA J.* **32**(8), 1598–1605 (1994)
- Menter, F.R., Kuntz, M., Langtry, R.: Ten years of industrial experience with the SST turbulence model. *Turbulence Heat Mass Transf.* **4**(1), 625–632 (2003)
- Moffatt, H.K.: Fluid dynamics. In: *The Princeton Companion to Applied Mathematics*, pp. 467–476. Princeton University Press (2015)
- Mokhtar, W., Hasan, M.: *A CFD Study of Wind Tunnel Wall Interference*. American Society for Engineering Education (2016, March)
- Muraoka, K., Okada, N., Kubo, D.: Quad tilt wing VTOL UAV: aerodynamic characteristics and prototype flight. In: *AIAA Infotech@ Aerospace Conference and AIAA Unmanned. Unlimited Conference*, p. 1834 (2009)
- Panagiotou, P., Kaparos, P., Yakinthos, K.: Winglet design and optimization for a MALE UAV Using CFD. *Aerosp. Sci. Technol.* **39**, 190–205 (2014)
- Panagiotou, P., Kaparos, P., Salpingidou, C., Yakinthos, K.: Aerodynamic Design of a MALE UAV. *Aerosp. Sci. Technol.* **50**, 127–138 (2016)
- Pattinson, J., Lowenberg, M.H., Goman, M.G.: Multi-degree-of-freedom wind-tunnel maneuver rig for dynamic simulation and aerodynamic model identification. *J. Aircr.* **50**(2), 551–566 (2013)
- Perzon, S.: On Blockage Effects in Wind Tunnels—A CFD Study (No. 2001-01-0705). SAE Technical Paper (2001)
- Pettersson, K., Rizzi, A.: Aerodynamic scaling to free flight conditions: past and present. *Prog. Aerosp. Sci.* **44**(4), 295–313 (2008)
- Ro, K., Raghu, K., Barlow, J.B.: Aerodynamic characteristics of a free-wing tilt-body unmanned aerial vehicle. *J. Aircr.* **44**(5), 1619–1629 (2007)

- Ross, I., Altman, A.: Wind tunnel blockage corrections: review and application to savonius vertical-axis wind turbines. *J. Wind Eng. Ind. Aerodyn.* **99**(5), 523–538 (2011)
- Schlichting, H., Gersten, K.: *Boundary Layer Theory*, 9th edn, p. 572. Springer, Berlin/Heidelberg (2016)
- Skalak, R., Ozkaya, N., Skalak, T.C.: Biofluid mechanics. *Annu. Rev. Fluid Mech.* **21**(1), 167–200 (1989)
- Stone, R.H.: Aerodynamic modelling of a wing-in-slipstream tail-sitter UAV. In: 2002 Biennial International Powered Lift Conference and Exhibit, p. 5951 (2002)
- Turbotek.: <https://www.turbotek.com.tr/egitim-amacli-ruzgar-tuneli-v2,2,16283#.X7h9m8gzaUk>. Accessed 10 Nov 2020 (n.d.)
- Ventura Diaz, P., Yoon, S.: High-fidelity computational aerodynamics of multi-rotor unmanned aerial vehicles. In: 2018 AIAA Aerospace Sciences Meeting, pp. 1–22 (2018)
- Vuruskan, A., Yuksek, B., Ozdemir, U., Yukselen, A., Inalhan, G.: Dynamic modeling of a fixed-wing VTOL UAV. In: 2014 International Conference on Unmanned Aircraft Systems (ICUAS), pp. 483–491. IEEE (2014)
- West, G.S., Apelt, C.J.: The effects of tunnel blockage and aspect ratio on the mean flow past a circular cylinder with Reynolds numbers between  $10^4$  And  $10^5$ . *J. Fluid Mech.* **114**, 361–377 (1982)
- Wilcox, D.C.: *Turbulence Modeling for CFD*, vol. 2, pp. 103–217. DCW Industries, La Canada (1998)
- Wisnoe, W., Nasir, R.E.M., Kuntjoro, W., Mamat, A.M.I.: Wind tunnel experiments and CFD analysis of Blended Wing Body (BWB) Unmanned Aerial Vehicle (UAV) at Mach 0.1 and Mach 0.3. In: International Conference on Aerospace Sciences and Aviation Technology, vol. 13, no. Aerospace Sciences & Aviation Technology, ASAT-13, May 26–28, 2009, pp. 1–15. The Military Technical College (2009, May)